

Phononic bandgap and phonon anomalies in HfN and HfN/ScN metal/semiconductor superlattices measured with inelastic x-ray scattering ^{EP}

Cite as: Appl. Phys. Lett. **117**, 111901 (2020); <https://doi.org/10.1063/5.0020935>

Submitted: 07 July 2020 . Accepted: 31 August 2020 . Published Online: 17 September 2020

Sourjyadeep Chakraborty ^{id}, Hiroshi Uchiyama ^{id}, Magnus Garbrecht ^{id}, Vijay Bhatia ^{id}, Ashalatha Indiradevi Kamalasanan Pillai, Joseph Patrick Feser ^{id}, Devashibhai T. Adroja, Sean Langridge ^{id}, and Bivas Saha ^{id}

COLLECTIONS

^{EP} This paper was selected as an Editor's Pick



View Online



Export Citation



CrossMark

Lock-in Amplifiers
up to 600 MHz



Phononic bandgap and phonon anomalies in HfN and HfN/ScN metal/semiconductor superlattices measured with inelastic x-ray scattering

Cite as: Appl. Phys. Lett. **117**, 111901 (2020); doi: [10.1063/5.0020935](https://doi.org/10.1063/5.0020935)

Submitted: 7 July 2020 · Accepted: 31 August 2020 ·

Published Online: 17 September 2020



View Online



Export Citation



CrossMark

Sourjyadeep Chakraborty,^{1,2,3}  Hiroshi Uchiyama,⁴  Magnus Garbrecht,⁵  Vijay Bhatia,⁵  Ashalatha Indiradevi Kamalasanan Pillai,⁵ Joseph Patrick Feser,⁶  Devashibhai T. Adroja,⁷ Sean Langridge,⁷  and Bivas Saha^{1,2,3,a)} 

AFFILIATIONS

¹Chemistry and Physics of Materials Unit, Jawaharlal Nehru Centre for Advanced Scientific Research, Bangalore 560064, India

²International Centre for Materials Science, Jawaharlal Nehru Centre for Advanced Scientific Research, Bangalore 560064, India

³School of Advanced Materials, Jawaharlal Nehru Centre for Advanced Scientific Research, Bangalore 560064, India

⁴Research and Utilization Division, Japan Synchrotron Radiation Research Institute (JASRI), SPring-8, 1-1-1 Koto, Sayo, Hyogo 679-5198, Japan

⁵Australian Centre for Microscopy and Microanalysis, The University of Sydney, Camperdown, New South Wales 2006, Australia

⁶Department of Mechanical Engineering, University of Delaware, Newark, Delaware 19716, USA

⁷ISIS facility, Rutherford Appleton Laboratory, Chilton, Oxon OX11 0QX, United Kingdom

^{a)} Author to whom correspondence should be addressed: bsaha@jncasr.ac.in and bivas.mat@gmail.com

ABSTRACT

Epitaxial metal/semiconductor superlattice heterostructures with lattice-matched abrupt interfaces and suitable Schottky barrier heights are attractive for thermionic energy conversion, hot electron-based solar energy conversion, and optical hyperbolic metamaterials. HfN/ScN is one of the earliest demonstrations of epitaxial single-crystalline metal/semiconductor heterostructures and has attracted significant interest in recent years to harness its excellent properties in device applications. Although the understanding of the mechanism of thermal transport in HfN/ScN superlattices is extremely important for their practical applications, not much attention has been devoted to measuring their phonon dispersion and related properties. In this Letter, we employ non-resonant meV-resolution inelastic x-ray scattering to determine the momentum-dependent phonon modes in epitaxial metallic HfN and lattice-matched HfN/ScN metal/semiconductor superlattices. HfN exhibits a large phononic bandgap (~ 40 meV) and Kohn anomaly in the longitudinal and transverse acoustic phonon modes at $q \sim 0.73$ along the [100] and [110] directions of the Brillouin zone due to the nesting of the Fermi surface by the wave vector (q). The in-plane [100] acoustic phonon dispersion of the HfN/ScN superlattices is found to be dominated by the HfN phonons, while the optical phonons exhibit both ScN and HfN characteristics. First-principles density functional perturbation theory modeling is performed to explain the experimental phonon spectra, and temperature-dependent thermal conductivity is measured using a pump-probe spectroscopic technique. These results will help understand the phonons in HfN and HfN/ScN metal/semiconductor superlattices for thermionic energy conversion.

Published under license by AIP Publishing. <https://doi.org/10.1063/5.0020935>

Ever since the pioneering theoretical proposal by Tsu and Esaki in the 1970s on “tunneling in finite superlattices,”¹ the development of epitaxial lattice-matched semiconductor superlattices such as GaAs/AlAs has fundamentally transformed research on heterostructure materials.^{2–4} Semiconductor superlattices have emerged as the most prominent artificially structured crystals and have found applications in the generation of electronic and optoelectronic devices as well as for

the fundamental physics and device engineering studies.^{5–8} However, there is a widespread realization in the scientific community that some of the most pressing challenges of our time, such as energy security, optical communication, thermo-photonic energy conversion, sensing, and imaging, require advanced heterostructure materials with improved functionalities. Epitaxial single-crystalline metal/semiconductor superlattices are a class of artificially structured materials that

may overcome some of the limitations of semiconductor superlattices.^{9,10} Lattice-matched abrupt interfaces and tunable Schottky barrier heights in metal/semiconductor superlattices enable thermionic emission-based thermoelectric devices with improved *figures-of-merit* (zT), hot electron-based photo-catalysis and photo-diodes with superior solar-energy conversion efficiencies, and optical hyperbolic metamaterials for engineering quantum electronic properties of materials.^{11–18} Theoretical studies have also predicted that metal/semiconductor superlattices should exhibit exotic thermo-photonic properties such as thermal hyper-conductivity and optical rainbow trapping, which are not possible to achieve with other materials.^{19,20}

Central to the development of such exciting devices is the need for an in-depth understanding of the energy (light, current, and heat) transport mechanisms in the metal/semiconductor superlattice metamaterials. While the optical and electronic transport studies are progressing at a rapid pace, a detailed understanding of the thermal transport mechanism in metal/semiconductor superlattices has been rather slow and based primarily on thermal conductivity measurements. For example, time domain thermoreflectance (TDTR) pump-probe-based cross-plane thermal conductivity measurements on TiN/Al_{0.72}Sc_{0.28}N metal/semiconductor superlattices have demonstrated a wave nature to particle-nature transition in the thermal transport and phonon filtering at metal/semiconductor interfaces.¹² With heavy tungsten (W) incorporation inside TiN layers in the form of alloys, the cross-plane thermal conductivity in Ti_{0.7}W_{0.3}N/Al_{0.72}Sc_{0.28}N superlattices was reduced to a small value of 1.7 W/m K at room temperature, which is necessary for achieving a high thermoelectric *figure-of-merit* (zT).²¹ Thermal conductivity measurements on ZrN/ScN metal/semiconductor superlattices also exhibited incoherent phonon boundary scattering at the superlattice interfaces and a reduction of the thermal conductivity with an increase in the interface densities.²² However, thermal conductivity originates from an average over all phonon modes and does not illustrate directly the momentum dependence of various phonon modes and their lifetimes, which are crucial for the understanding of a whole host of thermal properties. For example, the highest energy phonon mode at the zone center dominates the heat dissipation process of hot carriers, owing to the Fröhlich interaction.²³ Similarly, mismatches in the phonon density of states ($pDOS$) or the phononic bandgap are proposed to block the transmission of the mid-frequency range phonon modes in superlattices that reduce their thermal conductivity.²⁴ Therefore, motivated by the requirement to understand the momentum dependence of various phonon modes and their relationship with the thermal transport properties, in this Letter, we employed non-resonant meV-resolution inelastic x-ray scattering (IXS) to investigate the phonon dispersion in epitaxial metallic HfN and lattice-matched HfN/ScN metal/semiconductor superlattices.

HfN/ScN is one of the earliest demonstrations of epitaxial lattice-matched metal/semiconductor superlattices and is currently extensively researched to develop Schottky barrier-based thermionic emission converters.⁹ Previous density functional theory (DFT) modeling had predicted a Schottky barrier height of 0.17 eV at the HfN/ScN interfaces and a reduction of the thermal conductivity along the cross-plane directions.²⁵ Thermal stability analysis on epitaxial HfN/ScN superlattices deposited on MgO substrates showed that the superlattices are stable at high temperatures ($\sim 850^\circ\text{C}$) and exhibit dislocation-pipe diffusions at elevated temperatures.⁹ Pristine HfN, on the other hand, is a rock salt transition metal mono-nitride with high

melting temperature ($\sim 3300^\circ\text{C}$) and exhibits metallic-to-insulating electrical properties depending on its stoichiometry²⁶ and superconducting nature with a transition temperature of $\sim 8.2\text{K}$.²⁷ Sputter-deposited stoichiometric HfN films show gold-like metallic reflective surfaces and have found applications as diffusion barriers, as buffer layers in microelectronics, and thermoelectric and plasmonic materials.^{25–27} Recently, HfN has also become an attractive material for its potential hot-carrier solar cell applications and has exhibited a long photo-excited carrier lifetime of up to a nanosecond that is related to its phonon properties.⁶ On the other hand, ScN is a well-established rock salt indirect bandgap semiconductor, which has attracted significant interest for thermoelectric applications,^{28,29} as a substrate for defect-free GaN growth,^{30–32} and for Al_{1-x}Sc_xN piezoelectric alloys for sensors and actuators.³³ Recent IXS studies by one of the co-authors on hybrid vapor phase epitaxy deposited ScN have demonstrated detailed phonon dispersion along the Γ -X direction and three body phonon-phonon interactions describing the optical phonon lifetime.³⁴ Therefore, in this work, IXS measurements of phonon dispersion and momentum-dependent phonon properties are presented for pristine HfN and HfN/ScN metal/semiconductor superlattices. Structural and microscopic properties of the films are characterized with x-ray diffraction and electron microscopy methods, while TDTR is used to measure the cross-plane thermal conductivity.

The pristine HfN thin film ($\sim 1\ \mu\text{m}$) and 6 nm/6 nm HfN/ScN metal/semiconductor superlattices with a total thickness of $\sim 1\ \mu\text{m}$ are deposited on (001) MgO substrates with reactive dc-magnetron sputtering at a base pressure of 2×10^{-8} Torr at a substrate temperature of 850°C . The details about the growth process are presented elsewhere.³⁵ Structural characterization of the films with high-resolution x-ray diffraction (HRXRD) with a wavelength of $1.54059\ \text{\AA}$ revealed that both HfN and HfN/ScN superlattices grow with (001) orientations on MgO substrates [see Fig. 1(a)]. The 002 peaks in HfN and HfN/ScN superlattices are located at 39.75° and 39.77° , respectively, in the XRD pattern, representing their c -axis lattice constant of $4.53\ \text{\AA}$ and $4.53\ \text{\AA}$, respectively. The measured lattice constant of HfN is consistent with previous literature reports.³⁶ In addition, as HfN is lattice-matched with ScN, a similar c -axis lattice constant in the HfN/ScN superlattice to that in HfN is also not surprising. The full-width-at-half-maxima (FWHM) of the rocking curve (ω -scan) for HfN [see the inset of Fig. 1(a) (upper panel)] and HfN/ScN superlattices [see the inset of Fig. 1(a) (lower panel)] are found to be 0.68° and 1.1° , respectively, which represent their mosaic spread and textured nominally single-crystalline growth. Four equally spaced asymmetric ϕ -peaks (not shown here) also show epitaxial growth of HfN and HfN/ScN on MgO substrates. The transmission Kikuchi diffraction (TKD) orientation map [Fig. 1(b)] and inverse pole figures [Figs. 1(c) and 1(d)] also exhibit no significant misorientations between HfN and HfN/ScN superlattices with MgO substrates (see the [supplementary material](#) for details).

Microstructural characterization with high-resolution scanning transmission electron microscopy (HRSTEM) reveals high-quality epitaxial and uniform HfN film growth on MgO substrates with atomically sharp HfN/MgO interfaces [see Fig. 2(c)]. HfN grows with a cube-on-cube (001)[001] HfN || (001)[001] MgO epitaxial relationship on MgO substrates and due to an $\sim 6\%$ – 7% lattice-mismatch between the HfN and MgO, misfit dislocations are visible at HfN/MgO interfaces [see Fig. 2(c)]. In addition, low contrast threading

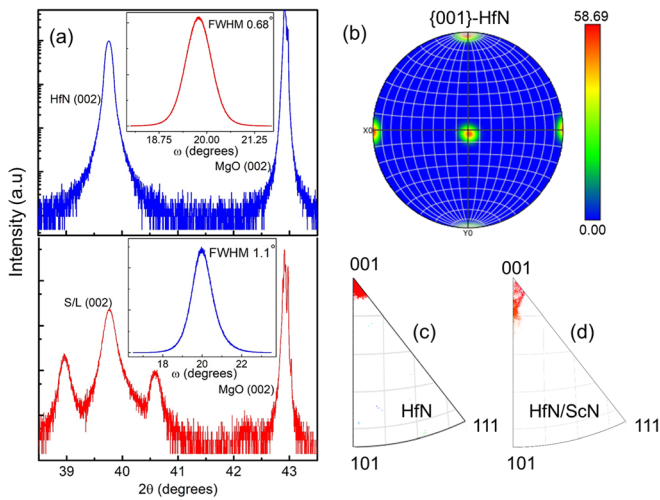


FIG. 1. (a) Symmetric 2θ - ω HRXRD patterns of HfN (upper panel) and HfN/ScN superlattices (lower panel) are presented. HfN and the superlattices grow with 002 orientations on (002) MgO substrates with a FWHM of the rocking curve (see the inset of Fig. 1(a)). Interference fringes are visible in the lower panel of Fig. 1(a). (b) Transmission Kikuchi diffraction pole figure (orientation map) of HfN showing no significant misorientation between HfN and MgO. Inverse pole figures of HfN (c) and HfN/ScN (d) superlattices show 001 oriented growth.

dislocations are also observed. The HfN films, however, do not show any voids or other types of extended defects that are generally observed in several other transition metal mono-nitrides.^{37,38} Low-magnification HRTEM images of HfN/ScN superlattices exhibit columnar growth with the columns separated by threading dislocations [Fig. 2(b)]. Within the columnar grains, layers are uniform with sharp and abrupt interfaces [see Fig. 2(d)]. The superlattice also exhibits a cube-on-cube (001)[001] HfN/ScN || (001)[001] MgO epitaxial relationship on the MgO substrate. Layers are curved towards the substrate due to the onset of dislocation-pipe diffusion at high growth temperatures.

IXS measurements are performed at BL35XU of the SPring-8 synchrotron facility with an incident x-ray energy ($h\omega$) of 21.474 keV, which corresponds to the Si (11 11 11) reflection and results in an energy resolution of 1.4–1.7 meV.³⁹ The use of 12 analyzer crystals on BL35XU allows 12 momentum transfers to be scanned simultaneously, which leads to highly efficient data collection. In the experimental setup, each analyzer has a momentum resolution of 0.9 nm^{-1} or $\Delta Q \sim (0.07, 0.07, 0.01) - (0.05, 0.05, 0.06)$ (depending on the geometry). The overall uncertainty in determining the IXS peak positions is approximately $\pm 0.2 \text{ meV}$. The incident x-ray angle (α) with respect to the surface of the film was optimized, and an angle of $\alpha = 0.4^\circ - 0.7^\circ$ was chosen so that the sensitivity to the film was maximized and the substrate contribution was minimized [see Fig. 3(a)]. The density functional perturbation theory (DFPT) calculations are performed with the generalized gradient approximation (GGA) and ultra-soft pseudopotentials as implemented in the Quantum Espresso code (see the [supplementary material](#) for details).

The IXS acoustic phonon spectrum of HfN at room temperature is presented in Fig. 3 for $Q \sim (3 - q, 1, 1)$ (right panel) and $(2 - q, 2 - q, 2)$ (left panel). These momenta correspond to

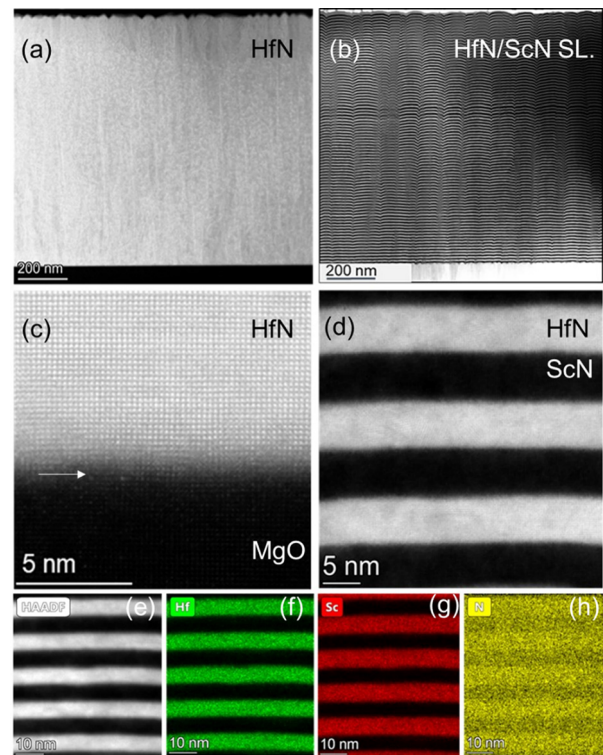


FIG. 2. (a) Low-magnification high-angle annular dark field scanning transmission electron microscopy (HAADF-STEM) image of an HfN thin film deposited on MgO (001) substrates. The figure shows high-quality uniform crystal growth without the presence of significant extended defects. (b) HfN/ScN metal/semiconductor superlattices deposited on the HfN buffer layer on the MgO substrate are presented. Superlattices exhibit some threading dislocations. (c) Atomic resolution-STEM image showing the HfN lattice epitaxially grown on the MgO substrate. The HfN/MgO interface appears clean and abrupt (white arrow in the figure). (d) HAADF-STEM image of the HfN/ScN superlattice that indicates HfN and ScN layers separated by clean and abrupt interfaces without much atomic mixing at the interfaces. (e) HAADF-STEM images of the superlattice and corresponding Hf (f), Sc (g), and N (h) elemental energy-dispersive x-ray spectroscopy (EDS) maps demonstrating well-separated layers without diffusion of atoms into adjacent layers. Due to the EDS peak overlap between the Sc-L edge and the N-K edge, N stoichiometry in ScN is less precise and results in the contrast difference in N intensity between ScN and HfN.

$q = (q00)$ ($\Gamma - X$ direction) and $(qq0)$ ($\Gamma - K$ direction) in the reduced Brillouin zone ($Q = q + G$, G is the reciprocal lattice vector) [see Fig. 3(b)]. The peak positions from the IXS spectrum [Fig. 3(c)] are determined using a Voigt peak fitting and plotted in Fig. 3(d) with black dots along with the acoustic phonon dispersion of HfN obtained from DFPT calculations. It is clear from Figs. 3(d) and 3(e) (log-scale intensity plot of experimental acoustic spectrum) that the calculated acoustic phonon spectrum agrees extremely well with the experimental HfN phonon modes and all of the observed modes are properly assigned with those calculated. For example, along the [100] directions, the acoustic phonon consists of two degenerate transverse acoustic (TA) modes and a longitudinal acoustic (LA) mode that is higher in energy as expected. Interestingly, the IXS spectrum exhibits a Kohn anomaly^{27,40} (anomalous dip in the LA modes) along the [100]

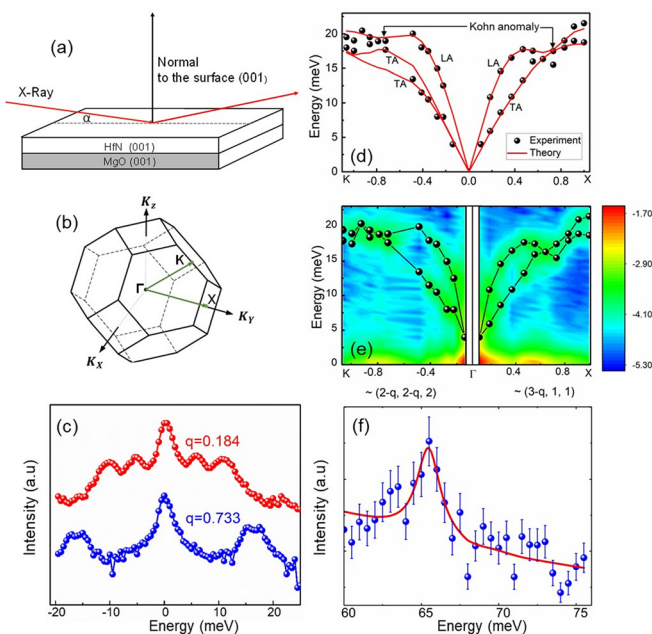


FIG. 3. (a) Schematic of the experimental IXS measurement. (b) Brillouin zone of the HfN crystal. The green arrows correspond to the direction of the measurements. (c) IXS acoustic phonon spectra (in log scale) of HfN near the Γ -point ($q = 0.18$) and at $q = 0.73$ where the observed Kohn anomaly is presented. (d) Experimental (black dots) acoustic phonon modes obtained from IXS spectra at various q points are presented along with the theoretically calculated (red lines) acoustic phonon dispersion. (e) IXS spectra on a logarithmic scale obtained for $Q \sim (3-q, 2-q, 2)$ (left panel) representing $\Gamma - X$ and $(3-q, 1, 1)$ (right panel) representing $\Gamma - K$ directions. (f) Optical phonon spectrum of HfN near the Γ point ($q = 0.18$) fitted with a Voigt profile. All the data in figure. (c)–(f) are measured at 300 K.

directions near $q = 0.73$ due to the nesting of the Fermi surface by the wave vector. Such a Kohn anomaly is also present along the [110] directions for both of the LA and TA modes. Both the IXS spectrum and the DFPT calculations show a reverse ordering of the LA and TA modes along the [100] after $q = 0.73$. The Kohn anomaly in superconducting metals such as HfN is well-known and has been previously observed in transition metal nitrides such as ZrN and NbN.^{38,40} First-principles DFT modeling and inelastic neutron scattering (INS) experiments on bulk HfN were performed previously to understand the relation between the superconductivity and phonon coupling in these materials, which are in agreement with our work^{27,40} albeit the spectral position. While in bulk HfN, INS showed the minima (Kohn anomaly) in LA at $q = 0.5$ along [001] and $q = 0.55$ along [011], the present IXS on the HfN film shows the corresponding minima at $q = 0.73$ along [001] and $q = 0.72$ along [011]. The IXS spectrum near the Γ -point as well as at $q = 0.73$ is presented in Fig. 3(c) that does not only show their respective LA and TA modes but also the Rayleigh or elastic scattering peak.

Unlike the acoustic phonon dispersion, the optical phonon of HfN in the IXS spectrum is rather weak and was only observed near the Γ -point of the Brillouin zone. Near the Γ -point, both the longitudinal optical (LO) and transverse optical (TO) phonons are degenerate and exhibit an energy of 65.4 meV (527 cm^{-1}) [see Fig. 3(f)], which is consistent with the Γ -point phonon energy calculated by DFPT. With

the increase in q away from the Γ -point, the LO and TO modes split as expected from the DFPT. However, due to the weak intensity, deconvolution of such IXS peaks was not possible. Nevertheless, the IXS spectrum and the DFPT analysis exhibit a large mismatch in the phonon density of states of $\sim 40 \text{ meV}$ (see Fig. S1 in the supplementary material) that is not only the largest among transition metal mononitrides^{41,42} but also among the largest reported for other types of materials^{43,44} such as h-BAs.⁴⁵ Such a large mismatch in p DOS results from the large mass mismatch between Hf (178.49) and N (14) atoms, which leads to a smaller vibrational frequency for the acoustic phonons. Due to such a large gap in the vibrational spectrum, HfN exhibits large lifetime of the photo-excited carriers as speculated previously and should be ideally suited for hot carrier solar cell applications.⁶ Unfortunately, the current measurements provide no estimation of the lifetime due to the low spectral intensity.

Room-temperature IXS of the HfN/ScN superlattices is conducted for $Q \sim (3 - q, 1, 1)$, i.e., $(q00)$ or the $\Gamma - X$ direction of the Brillouin zone, and representative spectra from several q -points are presented in Fig. 4(a). The measurement of the out-of-plane IXS was not possible due to the overlapping Bragg peaks arising from the superlattice reflections as well as due to the large mosaic spread in the superlattices. Acoustic phonon dispersion [see Fig. 4(b)] extracted from the IXS spectra [plotted in Fig. 4(a)] shows that the HfN/ScN acoustic phonon along the $\Gamma - X$ direction is dominated by HfN acoustic modes, which was also predicted by DFPT analysis³⁹ (with a very small system size of $\sim 1 \text{ nm}$ period thickness). As Hf is almost four times heavier than Sc atoms, low frequency acoustic modes in HfN/ScN superlattices are expected to be dominated by the heavy Hf atomic vibrations. Acoustic phonon velocity and Debye temperature of the superlattice along the $\Gamma - X$ direction, therefore, are also similar to HfN. In addition, the LA acoustic phonon mode [see Fig. 4(b)] exhibits the Kohn anomaly in superlattices, which was observed for pristine HfN. Several optical modes are also observed in the IXS [see Figs. 4(a) and 4(c)] with peaks that are larger in intensities close to the X-point of the Brillouin zone. Close to the Γ -point, optical phonons having the largest energy were found at $\sim 84 \text{ meV}$ that correspond to the ScN LO modes found previously.³³ The energy of this mode decreased with an increase in q [see Fig. 4(c)] and acquires a value of $\sim 60 \text{ meV}$ at the X point and a dispersion that resembles the ScN LO phonon modes. Optical phonons in the 50–60 meV energy range in superlattices result from the ScN TO optical modes as well as from the HfN LO and TO modes as shown. As the period thickness of the superlattice is $\sim 12 \text{ nm}$, along the in-plane $\Gamma - X$ direction, lattice vibration or phonons are expected to contain information from both of the materials, and superlattice modes (arising from interference effects) are unlikely to appear. Elastic constants, bulk modulus, and Debye temperature of HfN and HfN/ScN superlattices are further extracted from experimental phonon dispersions (see the supplementary material), which match with theoretical calculations.⁴⁶ In addition, to complement the IXS measurements, the thermal conductivity of HfN and HfN/ScN superlattices is further measured with TDTR,^{47–49} and detailed analysis of the results is presented in Sec. G of the supplementary material.

In conclusion, meV resolution inelastic x-ray scattering measurements are performed to determine the vibrational spectra of pristine metallic HfN and epitaxial nominally single-crystalline HfN/ScN metal/semiconductor superlattices to understand their phonon

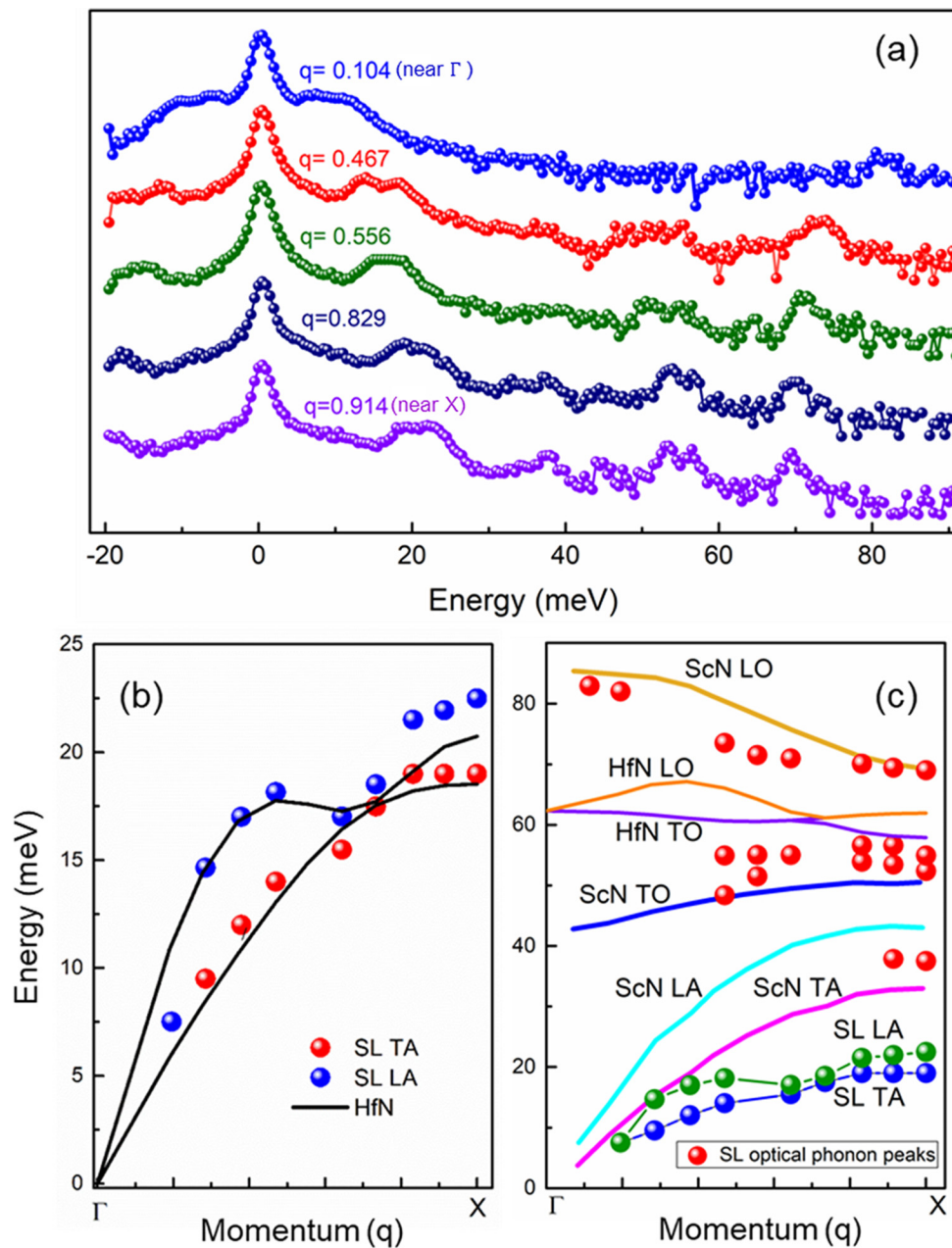


FIG. 4. Phonon dispersion of the HfN/ScN superlattice. (a) IXS spectra of HfN/ScN along the Γ -X [100] direction. (b) Acoustic phonon dispersion data along with HfN acoustic phonon from DFPT. (c) HfN/ScN superlattice optical and acoustic phonon peaks extracted from the IXS are presented as circles. Lines are drawn to show the HfN and ScN thin film phonon modes.

properties for thermoelectric as well as hot-carrier solar energy conversion. HfN exhibits a low energy acoustic phonon and a large gap between the acoustic and optical phonon modes that result from the mismatches in the atomic mass of Hf and N. The low energy acoustic phonon in HfN results in a smaller lattice thermal conductivity, and the high optical phonon energy coupled with the mismatches in pDOS

enables it to retain hot carriers for longer times. In addition, Kohn anomalies in the LA and TA modes are also observed in HfN as well as in HfN/ScN metal/semiconductor superlattices. The acoustic phonon spectrum of the superlattices is found to be dominated by Hf atomic vibrations in HfN, while optical phonons result from both HfN and ScN. These results will be important for understanding the

thermal properties of HfN and HfN/ScN metal/semiconductor superlattices and will help designing thermoelectric, thermionic, and hot-carrier solar energy conversion devices with improved efficiencies.

See the [supplementary material](#) for information related to the inelastic x-ray scattering measurements, computational and transmission Kikuchi diffraction studies, interface roughness of the superlattices, elastic constant of the materials, and thermal conductivity measurements.

S.C. and B.S. acknowledge the International Center for Materials Science (ICMS) and Sheikh Saqr Laboratory (SSL) in JNCASR for support. Measurements in SPring-8 are performed with Proposal No. 2019B1127. S.C. and B.S. thank Synchrotron and Neutron Project No. 2019/IN-010 from Nano-mission of the Department of Science and Technology, India, supporting the travel and logistics. B.S. acknowledges the Science and Engineering Research Board (SERB) of the Government of India, Start-Up Research Grant No. SRG/2019/000613 for financial support. The authors thank the Department of Science and Technology, India (SR/NM/Z-07/2015) for the financial support and Jawaharlal Nehru Centre for Advanced Scientific Research (JNCASR) for managing the project.

DATA AVAILABILITY

Data available on request from the authors.

REFERENCES

- ¹R. Tsu and L. Esaki, *Appl. Phys. Lett.* **22**, 562 (1973).
- ²G. Bratina, L. Sorba, A. Antonini, L. Vanzetti, and A. Franciosi, *J. Vac. Sci. Technol., B* **9**, 2225 (1991).
- ³M. N. Luckyanova, J. A. Johnson, A. A. Maznev, J. Garg, A. Jandl, M. T. Bulsara, E. A. Fitzgerald, K. A. Nelson, and G. Chen, *Nano Lett.* **13**, 3973 (2013).
- ⁴S. Adachi, *J. Appl. Phys.* **58**, R1–R29 (1985).
- ⁵G. Xiao, G. Zheng, M. Qiu, Q. Li, D. Li, and M. Ni, *Appl. Energy* **208**, 1318 (2017).
- ⁶S. Chung, X. Wen, S. Huang, N. Gupta, G. Conibeer, S. Shrestha, T. Harada, and T. W. Kee, *Sol. Energy Mater. Sol. Cells* **169**, 13 (2017).
- ⁷C. Berthod, N. Binggeli, and A. Baldereschi, *Phys. Rev. B* **68**, 085323 (2003).
- ⁸H. Xia, R. Patterson, S. Smyth, Y. Feng, S. Chung, Y. Zhang, S. Shrestha, S. Huang, H. Uchiyama, S. Tsutsui, M. Sugiyama, A. Q. R. Baron, and G. Conibeer, *Appl. Phys. Lett.* **110**, 043102 (2017).
- ⁹B. Saha, A. Shakouri, and T. D. Sands, *Appl. Phys. Rev.* **5**, 021101 (2018).
- ¹⁰V. Rawat, Y. K. Koh, D. G. Cahill, and T. D. Sands, *J. Appl. Phys.* **105**, 024909 (2009).
- ¹¹A. G. Mal'shukov, Z. Ma, V. B. Antonyuk, and K. A. Chao, *Solid State Commun.* **119**, 563 (2001).
- ¹²S. Nayak, S. Acharya, M. Baral, M. Garbrecht, T. Ganguli, S. M. Shivaprasad, and B. Saha, *Appl. Phys. Lett.* **115**, 251901 (2019).
- ¹³M. Garbrecht, I. McCarroll, L. Yang, V. Bhatia, B. Biswas, D. Rao, J. M. Cairney, and B. Saha, *J. Mater. Sci.* **55**, 1592 (2020).
- ¹⁴S. K. Dutta, S. K. Mehetor, and N. Pradhan, *J. Phys. Chem. Lett.* **6**(6), 936–944 (2015).
- ¹⁵L. Ma, S. Chen, Y. Shao, Y. L. Chen, M. X. Liu, H. X. Li, Y. L. Mao, and S. J. Ding, *Catalysts* **8**(12), 634 (2018).
- ¹⁶N. Wu, *Nanoscale* **10**, 2679 (2018).
- ¹⁷O. Wada, H. Nobuhara, H. Hamaguchi, T. Mikawa, A. Tackeuchi, and T. Fujii, *Appl. Phys. Lett.* **54**, 16 (1989).
- ¹⁸M. Zirngibl and M. Ilegems, *J. Appl. Phys.* **69**, 8392 (1991).
- ¹⁹B. Saha, Y. R. Koh, J. Comparan, S. Sadasivam, J. L. Schroeder, M. Garbrecht, A. Mohammed, J. Birch, T. Fisher, A. Shakouri, and T. D. Sands, *Phys. Rev. B* **93**, 045311 (2016).
- ²⁰M. S. Jang and H. Atwater, *Phys. Rev. Lett.* **107**, 207401 (2011).
- ²¹B. Saha, Y. R. Koh, J. P. Feser, S. Sadasivam, T. S. Fisher, A. Shakouri, and T. D. Sands, *J. Appl. Phys.* **121**, 015109 (2017).
- ²²B. Saha, T. D. Sands, and U. V. Waghmare, *J. Appl. Phys.* **109**, 073720 (2011).
- ²³J. Fu, Q. Xu, G. Han, B. Wu, C. H. A. Huan, M. L. Leek, and T. C. Sum, *Nat. Commun.* **8**(1), 1300 (2017).
- ²⁴V. Narayanamurti, H. L. Störmer, M. A. Chin, A. C. Gossard, and W. Wiegmann, *Phys. Rev. Lett.* **43**, 2012 (1979).
- ²⁵B. Saha, T. D. Sands, and U. V. Waghmare, *J. Phys.: Condens. Matter* **24**, 415303 (2012).
- ²⁶H. A. Jehn, U. Kopacz, and S. Hofmann, *J. Vac. Sci. Technol., A* **3**, 2406 (1985).
- ²⁷A. N. Christensen, W. Kress, M. Miura, and N. Lehner, *Phys. Rev. B* **28**(2), 977 (1983).
- ²⁸B. Biswas and B. Saha, *Phys. Rev. Mater.* **3**, 020301 (2019).
- ²⁹P. Eklund, S. Kerdsonpanya, and B. Alling, *J. Mater. Chem. C* **4**, 3905 (2016).
- ³⁰C. F. Johnston, M. A. Moram, M. J. Kappers, and C. J. Humphreys, *Appl. Phys. Lett.* **94**, 161109 (2009).
- ³¹M. A. Moram, C. F. Johnston, M. J. Kappers, and C. J. Humphreys, *J. Cryst. Growth* **311**, 3239 (2009).
- ³²M. A. Moram, M. J. Kappers, T. B. Joyce, P. R. Chalker, Z. H. Barber, and C. J. Humphreys, *J. Cryst. Growth* **308**, 302 (2007).
- ³³R. Matloub, M. Hadad, A. Mazzalai, N. Chidambaram, G. Moulard, C. S. Sandu, T. Metzger, and P. Muralt, *Appl. Phys. Lett.* **102**, 152903 (2013).
- ³⁴H. Uchiyama, Y. Oshima, R. Patterson, S. Iwamoto, J. Shiomi, and K. Shimamura, *Phys. Rev. Lett.* **120**(23), 235901 (2018).
- ³⁵M. Garbrecht, J. L. Schroeder, L. Hultman, J. Birch, B. Saha, and T. D. Sands, *J. Mater. Sci.* **51**, 8250 (2016).
- ³⁶R. A. Araujo, X. Zhang, and H. Wang, *J. Vac. Sci. Technol., B* **26**, 1871 (2008).
- ³⁷T. D. Moustakas, *Phys. Status Solidi A* **210**, 169 (2013).
- ³⁸V. Potin, P. Vermaut, P. Ruterana, and G. Nouet, *J. Electron. Mater.* **27**, 266 (1998).
- ³⁹A. Q. R. Baron, Y. Tanaka, S. Goto, K. Takeshita, T. Matsushita, and T. Ishikawa, *J. Phys. Chem. Solids* **61**, 461 (2000).
- ⁴⁰R. Heid, K. P. Bohnen, B. Renker, T. Wolf, and H. Schober, *Phys. Rev. B* **71**(9), 092302 (2005).
- ⁴¹B. Saha, J. Acharya, T. D. Sands, and U. V. Waghmare, *J. Appl. Phys.* **107**, 033715 (2010).
- ⁴²E. I. Isaev, S. I. Simak, I. A. Abrikosov, R. Ahuja, Y. K. Vekilov, M. I. Katsnelson, A. I. Lichtenstein, and B. Johansson, *J. Appl. Phys.* **101**, 123519 (2007).
- ⁴³D. G. Cahill, W. K. Ford, K. E. Goodson, G. D. Mahan, A. Majumdar, H. J. Maris, R. Merlin, and S. R. Phillpot, *J. Appl. Phys.* **93**, 793 (2003).
- ⁴⁴D. G. Cahill, P. V. Braun, G. Chen, D. R. Clarke, S. Fan, K. E. Goodson, P. Keblinski, W. P. King, G. D. Mahan, A. Majumdar, H. J. Maris, S. R. Phillpot, E. Pop, and L. Shi, *Appl. Phys. Rev.* **1**, 011305 (2014).
- ⁴⁵G. Qin, Z. Qin, H. Wang, and M. Hu, arXiv preprint [arXiv:1904.00329](https://arxiv.org/abs/1904.00329) (2019).
- ⁴⁶A. Srivastava and B. D. Diwan, *Can. J. Phys.* **92**, 1058 (2014).
- ⁴⁷K. Kang, Y. K. Koh, C. Chiritescu, X. Zheng, and D. G. Cahill, *Rev. Sci. Instrum.* **79**, 114901 (2008).
- ⁴⁸D. G. Cahill, *Rev. Sci. Instrum.* **75**, 5119 (2004).
- ⁴⁹Y. K. Koh, S. L. Singer, W. Kim, J. M. O. Zide, H. Lu, D. G. Cahill, A. Majumdar, and A. C. Gossard, *J. Appl. Phys.* **105**, 054303 (2009).